LES OF SWIRLED TURBULENT FLOW IN ROD-BUNDLE USING IMMERSED BOUNDARY METHOD

Tsutomu Ikeno
Nuclear Fuel Industries,Ltd
950, Asashiro Nishi, 1-Chome, Kumatori-Cho Sennan-Gun, Osaka, 590-0481, Japan
t-ikeno@nfi.co.jp

Takeo Kajishima
Department of Mechanical Engineering,
Osaka University
Yamadaoka, Suita, Osaka, 565-0871, Japan
kajisima@mech.eng.osaka-u.ac.jp

ABSTRACT

In our LES, an improved immersed boundary method and a new one-equation dynamic SGS model was applied for accurate simulation of complicated wall boundary of industrial interest. Our computational results reasonably reproduced previous data obtained by experiments and computations. The results were able to represent the effect of flow geometry: the flow around the mixing-vane causes the swirl and the large-scale fluctuation enhancing heat transfer; turbulence stress promotes the decay of the swirl more strongly than in a pipe; but it produces a vortex in rod gap enhancing enthalpy mixing between channels. These results suggested that LES technique become a useful tool for designing the spacer grid by predicting the effect of flow control.

INTRODUCTION

The mainstream is in the axial direction of bundled rods, but the flow is distorted by spacer elements. As shown in Fig.1, the mixing-vanes attached at the spacer grids produces the swirl for enhancing heat transfer at the rod surfaces. To upgrade the thermal performance drastically, the optimization of swirl flow is necessary. For such a purpose, we believe the numerical simulation is useful to predict the effect of mixing-vane configuration on the flow and heat

Various efforts were thus made for the investigation about the swirl downstream of grid spacers, for example: the cross-sectional flow pattern was simulated well by RANS (In, 2003) and was successfully visualized with PIV technique (McClusky, 2002). However, we think that the swirl is much affected by the turbulence stress and that RANS or experiment is enough for the complete explanation. Our LES for the flow in bare rod-bundle successfully reproduced the geometrical effect that the turbulence energy in the main flow was transferred largely into the circumferential direction in the rod gap (Ikeno, et al., 2003a). The results indicated the possibility of LES as a support tool.

The geometry characteristic of rod-bundle causes difficulty in high-quality grid generation, due to azimuthally varying channel-width as well as the complexity of spacer grid. In our previous work (Ikeno, et al., 2003a), an efficient numerical procedure was developed for the immersed boundary method proposed by Mohd-Yusof (1997). Then we applied LES to the fully-developed turbulent flow using the Cartesian grid system.

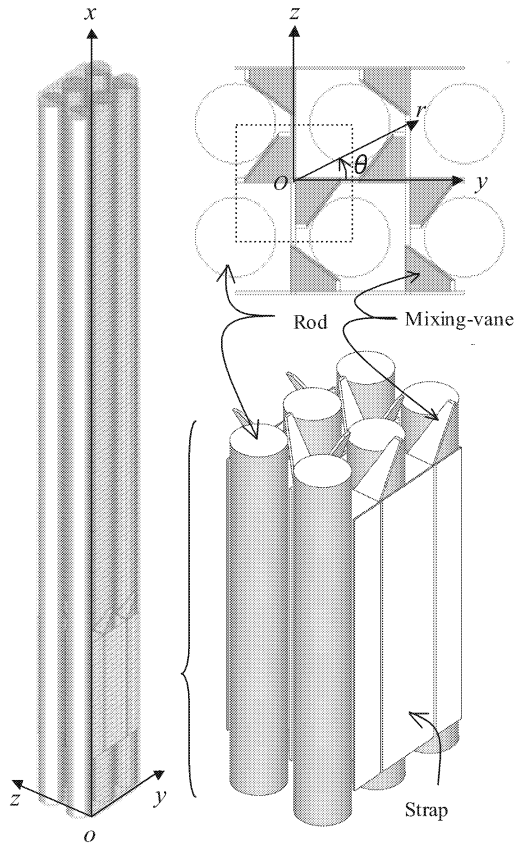

Figure 1: (a) Computational domain and a part of grid (every 8th grid is shown for each direction), (b) configuration of spacer grids and the area (doted square) for spatial average. This domain with periodical condition for every direction simulates a whole rod bundle. The coordinate system $o-xyz$ is used for instantaneous and $O-xr\theta$ for averaged results. The main flow is in the x-direction.

In this study, an improved immersed boundary method and a new one-equation dynamic SGS model are introduced to improve the accuracy of turbulence simulation in a complicated wall-boundaries: a higher-order forcing method (Ikeno, et al, 2003b) and a finite-difference formula of Poisson equation (Ikeno, et al, 2004) for accuracy and consistency for velocity and pressure; a dynamic procedure applied to the production term in the transport equation of SGS kinetic energy (Kajishima, 2003). Thus, our LES technique in couple with the immersed boundary method is applied for investigation of the geometry effect focusing on the development of the swirl.

NUMERICAL METHODS

The schematics of our immersed boundary method are shown in Fig.2. Our method consists of the higher-order forcing and the consistent correction as explained bellow.

Higer-order forcing method

In the immersed boundary methods, the following enforcement is applied to the right-hand side of momentum equation (Mohd-Yusof, 1997):

$$f_i = -RHS + \frac{\left(U_i^{n+1} - u_i^n\right)}{\Delta t} \tag{1}$$

where RHS denotes the right-hand side of momentum equation; Δt is time increment. For the no-slip condition on the wall, the desired velocity U_i^{n+1} is given by the interpolation between zero on the wall and the value at adjacent grid point. We represent U_i^{n+1} as follows:

$$U_i^{n+1} = \varphi\left(u_i^{n+1}\right) \qquad at \qquad \mathbf{x}_i = \mathbf{b}_i \tag{2}$$

where $\mathbf{x}_i$ and $\mathbf{b}_i$ are the location vectors for the grid points for the component-i on the staggered grid system. By applying the higher-order forcing method (Ikeno, et al, 2003b) to 3-dimensional geometry, the interpolation function $\varphi(\phi_i)$ for arbitrary flux ϕ_i is reduced as follows:

$$\left[\varphi(\phi_i)\right]_{I,J,K} = \sum_{f,g,h}^{-2,2} A_i^{f,g,h} \left[\phi_i\right]_{I+f,J+g,K+h} \tag{3}$$

where (I, J, K) represents grid number for $\mathbf{b}_i$ and $\mathbf{b}_i$ is set at the grid point nearest to the wall. The coefficient $A_i^{f,g,h}$ is used for the interpolation for the component-i at the grid point (I, J, K) between zero at wall and ϕ_i at the adjacent grid

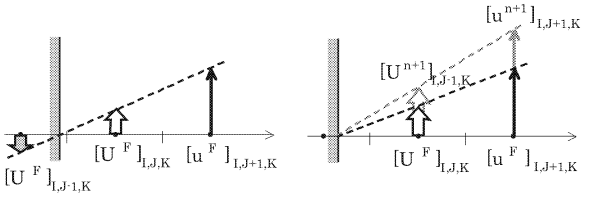

(a) (b)

Figure 2: The schematics of higher-order and consistent immersed boundary method. (a) Higher-order forcing to maintain the accuracy of velocity gradient at the wall. (b) Consistent correction of fractional step to obtain the no-slip condition at a new time step. The forcing is applied to all of the velocity components.

$(I + f, J + g, K + h)$. The higher-order method maintains the accuracy of the velocity gradient at the wall by the forcing at the points inside and outside the body, as shown in Fig.2(a). The points of $f, g, h = \pm 1$ and $f, g, h = \pm 2$ are used for the forcing outside and inside the body, respectively to avoid numerical instability (Ikeno, et al, 2003b).

Consistent correction method

In order to maintain the mathematical consistency between the numerical scheme and physical no-slip condition, we have derived the following procedure for time integration (Ikeno, et al, 2004). Firstly, the fractional step u_i^F is obtained by solving the following equation:

$$\left[1 - \frac{\Delta t\nu}{2}\delta_{x_j}\delta_{x_j} - \delta\left(\mathbf{x}_i - \mathbf{b}_i\right)\left(\varphi - \frac{\Delta t\nu}{2}\delta_{x_j}\delta_{x_j}\right)\right] u_i^F = \left[1 - \delta\left(\mathbf{x}_i - \mathbf{b}_i\right)\right] \times \left(u_i^n + \frac{\Delta t}{2}\left(3H_i^n - H_i^{n-1}\right) + \frac{\Delta t\nu}{2}\delta_{x_j}\delta_{x_j}u_i^n + \Delta t G_i\right) \tag{4}$$

where δ_{x_i} indicates central difference; H_i includes convective term and SGS stress term; the energy-conservation formula of the second-order finite-difference method (Kajishima, 1994) is particularly applied to the former; $\delta\left(\mathbf{x}_i - \mathbf{b}_i\right)$ is the delta function (denotes 1 when $\mathbf{x}_i = \mathbf{b}_i$, otherwise 0); G_i is the pressure gradient to drive the flow. Equation (4) is based on the Crank-Nicolson method for molecular viscous term and the Adams-Bashforth method for nonlinear terms. By storing the coefficients of the left-hand side prior to the time-integration, the procedure of categorization and interpolation for desired velocities is not required in each time step. This improves the efficiency of LES in extremely complex geometries.

If every stencil in Equation (4) does not include the immersed boundary ($\mathbf{x}_i \neq \mathbf{b}_i$), Equation (4) represents usual momentum equation. On the other hand, if any stencil in Equation (4) includes the immersed boundary ($\mathbf{x}_i = \mathbf{b}_i$), it represents the fractional step for the desired velocity:

$$U_i^F = \varphi\left(u_i^F\right) \qquad at \qquad \mathbf{x}_i = \mathbf{b}_i \tag{5}$$

Then the pressure gradient is added to advance a time step as follows:

$$u_i^{n+1} = u_i^F - \Delta t\left[1 - \delta\left(\mathbf{x}_i - \mathbf{b}_i\right)\right]\delta_{x_i}p^{n+1} - \Delta t\delta\left(\mathbf{x}_i - \mathbf{b}_i\right)\varphi\left(\delta_{x_i}p^{n+1}\right) \tag{6}$$

This equation maintains the no-slip condition on the wall by reducing Equation (5) to Equation (2). Hence, p in Equation (6) is obtained by solving the following Poisson equation:

$$\delta_{x_j}\delta_{x_j}p^{n+1} - \delta_{x_i}\left[\delta\left(\mathbf{x}_i - \mathbf{b}_i\right)\left(1 - \varphi\right)\delta_{x_i}p^{n+1}\right] = \frac{1}{\Delta t}\delta_{x_i}u_i^F \tag{7}$$

which is derived by the continuity restriction ($\delta_{x_i}u_i^{n+1} = 0$).

In Equations (4), (6) and (7), all spatial derivatives are approximated by the central difference formula of the second-order accuracy. The time integration is by the first-order fractional step method; this accuracy cannot be improved by any modification of boundary condition for fractional step u_i^F (Perot, 1993). The idea of our method is not an attempt for improving such temporal accuracy but for maintaining the consistency between the no-slip condition and the treatment

for velocity and pressure. Fig.2(b) indicates that such consistent pressure gradient corrects the pseudo no-slip condition for fractional step into the actual one for the new step. For example, the result of LES without the second term in the left-hand side of Equation (7) indicated higher flow rate because the immersed wall permits flow penetration due to the pressure gradient affected incorrectly by the solid body (Ikeno, et al, 2004).

In this study, Equations (4) and (7) are solved by successive over relaxation (SOR) method within 50 iterations. In this case, we confirmed the ratio between the norm of residual and that of the right hand side is approximately 10^{-5}. Since the second term in Equation (7) modifies the diagonal component of coefficient-matrix, the SOR method requires much iteration numbers until the convergence to machine-zero. However, we think SOR is one of the best selections, considering a minimum memory and numerical stability.

NUMERICAL RESULTS

The Reynolds number based on bulk velocity u_m, rod pitch P and kinematic viscosity ν is approximately 4100. To maintain the Reynolds number around this value, adjusted values are given for the pressure gradient in Equation (4):

$$G_i = 4\delta_{i1} u_\tau^2 / D_H \tag{8}$$

Here, δ_{i1}, u_τ and D_H are Kronecker delta, average friction velocity and the hydraulic equivalent diameter, respectively. The following results are normalized by P for length and u_τ for velocity.

Drag coefficients

The drag coefficients are calculated and compared with experiments in Fig.3. The drag coefficient in rod-bundle is based on the pressure loss obtained by subtracting the friction loss in bare rod-bundle from total loss in rod-bundle with spacer grid (Rehme, 1973). The friction loss was discussed in our previous work (Ikeno, et al, 2003a). We calculate the drag coefficient using the bulk velocities for this study and for bare rod-bundle of the same computational condition: one-equation dynamic SGS model (Kajishima, 2003), mesh spacing and pressure gradient. The grid spacer used in the experiment of Yang (1996) is a split-vane type as is simulated in our LES; but that of Rehme (1973) is different from both Yang's and ours. However, the data is useful for the comparison because it covers low Reynolds number region for Yang's (1996). Our numerical

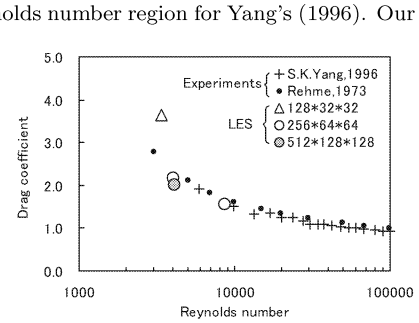

Figure 3: Comparison of form loss coefficients between LES and experiments. The result of LES includes various mesh numbers: $128 \times 64 \times 64$, $256 \times 128 \times 128$ and $512 \times 256 \times 256$ for x, y and z direction.

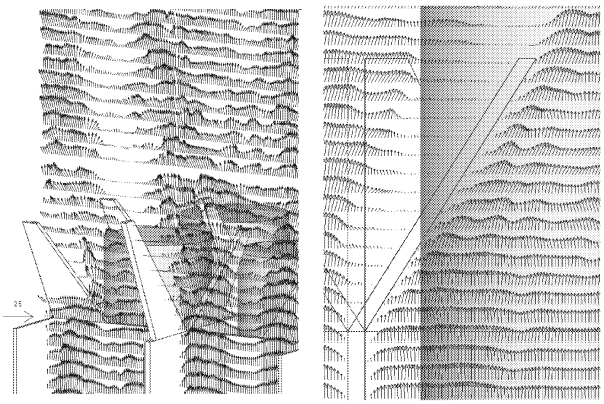

(a) (b)

Figure 4: Instantaneous velocity vectors around the spacer grid. (a) 3-dimensional vectors (u, v, w) in the $x - z$ plane at $y = 0.18$ across a mixing-vane (every 2nd grid is shown). (b) 2-dimensional vectors (u, v) in the $x - y$ plane at $z = 0.11$ across a mixing-vane (every grid is shown).The reference arrow indicates $25u_\tau$.

results converge to the experimental results as the mesh resolution becomes fine. Hereafter, we use the result of the finest mesh resolution: $512 \times 256 \times 256$ for x, y and z direction.

Velocity field around the spacer grid

The instantaneous velocity vectors are shown in Fig.4. Fig.4(a) indicates that the swirl observed is caused by the flow around the mixing-vane. This swirl contains large-scale fluctuation and affects the downstream turbulence. The scale of this unsteady phenomenon is important because it will promote heat transfer on the rod surface. As shown in Fig.4(b), the velocity field around a inclined plate is captured reasonably by our immersed boundary method and any numerical disturbance is not observed.

Mean streamwise velocities

Axial variations of mean streamwise velocities are shown in Fig.5. Hereafter, mean values are those averaged temporally during $5t^*$ after the flow developed and spatially in the area shown in Fig.1(b) for adjacent congruent area. Here, t^* is dimensionless time normalized by P/u_τ. The time increment is $0.0001t^*$. The points at $r > 0.357$ are inside the rod. The planes at $x = 2.3$ and $x = 5.1$ are insides the strap of the spacer grid: the values for 0 and 90 degrees are zero inside the body; the flows for 45 and -45 degrees are faster than those in any elevations because of the acceleration through the suddenly narrowing channel in the grid spacer; the position of local maximum of velocity is close to the corner between crossing straps at $x = 2.3$ and to the rod surface at $x = 5.1$. The plane at $x = 6.5$ is midpoint of the mixing-vanes: for 0 and 45 degree, the velocity profiles are sink at the center by the effect of strap upstream; for 90 and -45 degrees, the flow is slow behind the mixing-vane; especially the flow for 90 degrees is locally accelerated in the narrow region between the rod and the tip of mixing-vane. The planes from $x = 7.9$ to $x = 22$ are downstream of spacer grid: the profiles for 0 and 90 degrees and for 45 and -45 degrees approach those in shear-free condition and those in no-slip condition, respectively.

Turbulence intensities

Axial variations of turbulence intensities are shown in Fig.6. The turbulence intensity is based on the deviation from the corresponding component of mean velocity. The streamwise components are dominant at $x = 2.3$ and $x = 5.1$: the values for 0 and 90 degrees are zero inside the body; the streamwise components for 45 and -45 degrees are strong in the center at $x = 2.3$ because of the fast flow attacking to the strap and are diffused downstream at $x = 5.1$. The turbulence stresses are generally isotropic at $x = 6.5$: active turbulence diffusion is retrieving the velocity profile; especially the lateral fluctuation around $r = 0.3$ for 90 degrees corresponds to the origin of the swirl near the tip of a mixing-vane. From $x = 7.9$ to $x = 22$, the profiles for 0 and 90 degrees and for 45 and -45 degrees approach those in shear-free condition and those in no-slip

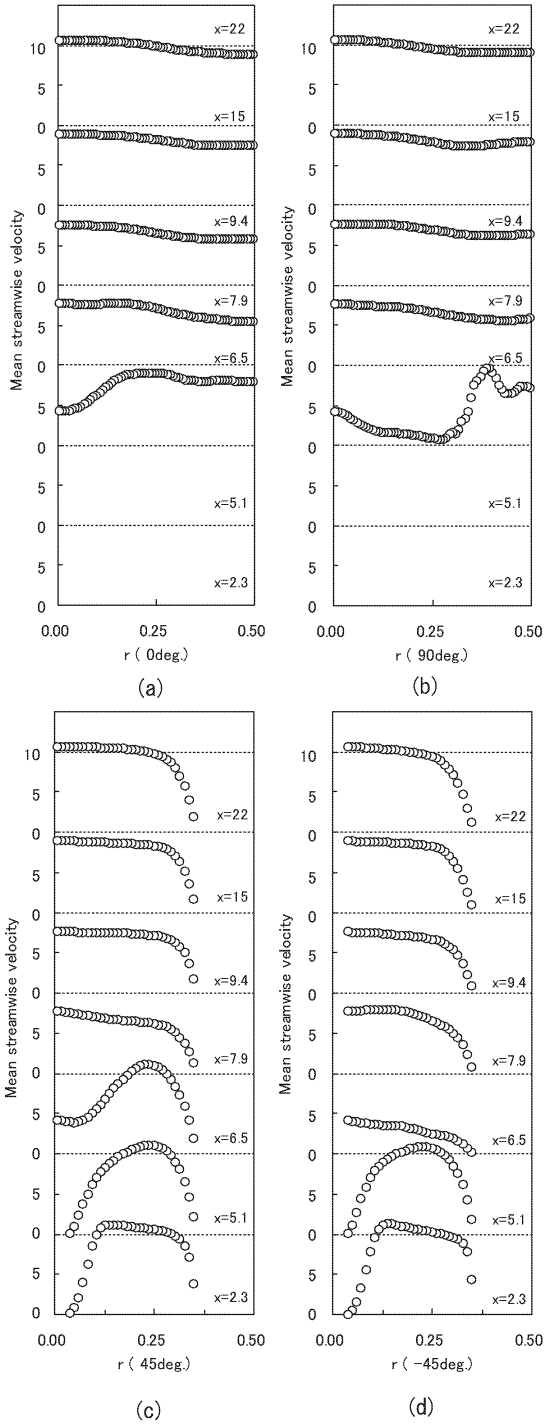

Figure 5: Axial variations of mean streamwise velocities: $\overline{u_x}$. $\theta =$ (a) 0, (b) 90, (c) 45 and (d) -45 in degree.

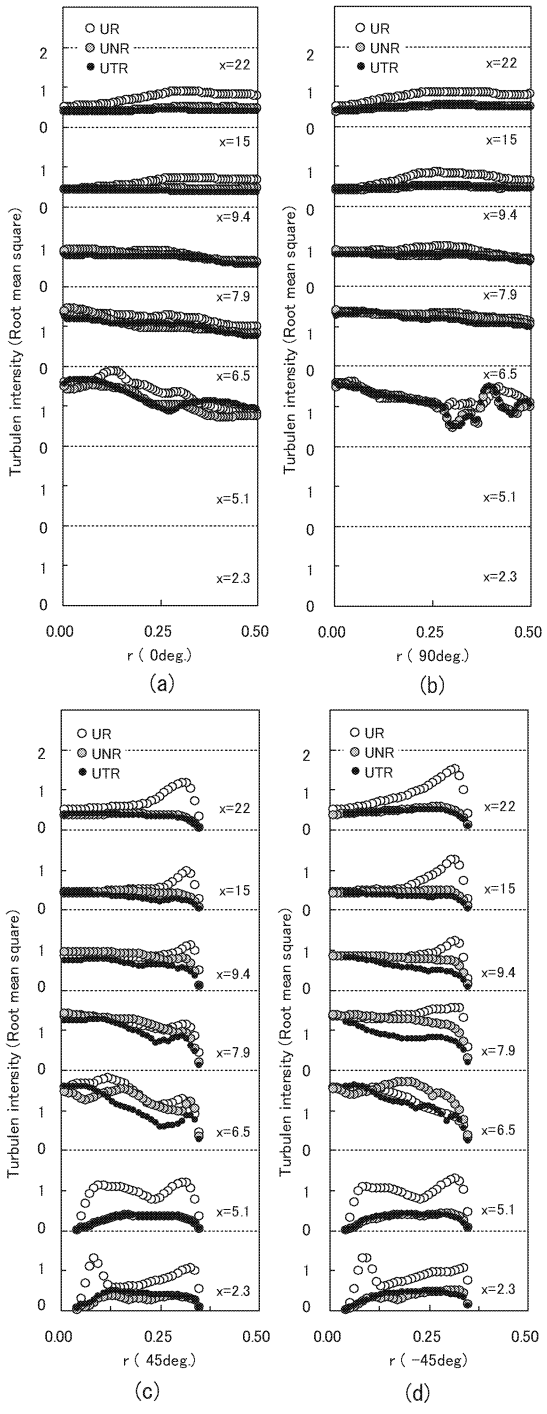

Figure 6: Axial variations of turbulence intensities: $\sqrt{\overline{u_x'^2}}$, $\sqrt{\overline{u_r'^2}}$ and $\sqrt{\overline{u_\theta'^2}}$ indicated by UR, UNR and UTR, respectively. $\theta =$ (a) 0, (b) 90, (c) 45 and (d) -45 in degree.

condition, respectively.

Decay of swirl

Mean lateral flow pattern is shown in Fig.7. The flow pattern is generally similar to the results of the computation by In (2003) and the measurement by McClusky (2002). This flow pattern is that of the swirl downstream of spacer grid. The arrangement of mixing-vanes in our LES is the same as that in McClusky (2002): it isolates the swirl in a channel among 4 rods. The swirl decreases as a function of the distance from the mixing-vanes. The prediction of this decrease rate is quite important to evaluate heat transfer at the rod surface.

Axial variation of mean angular momentum is shown in Fig.8. In this figure, the result of our LES is compared with experimental results for the swirl in a rod-bundle (McClusky, 2002) and in a pipe (Kreith and Sonju, 1965). The definition of angular momentum is:

$$\Omega = \iint_S r\overline{u_\theta} dS / \iint_S dS \tag{9}$$

where S is the region bounded by the circle: $r \leqq 0.35$. The LES agrees well with the experiment for the rod-bundle. The decrease in rod-bundle is significant near the mixing-vanes, but camparable data is not found in the experiment. The decay of the swirl in a rod-bundle is faster than that in a pipe. We think this is the effect of turbulence stress. McClusky (2002) investigated the lateral velocity profiles of decaying swirl by using an analogy with Lamb-Oseen vortex but did not show the contribution of turbulence stress. Our LES can provide such data and we discuss the decaying swirl by developing his approach.

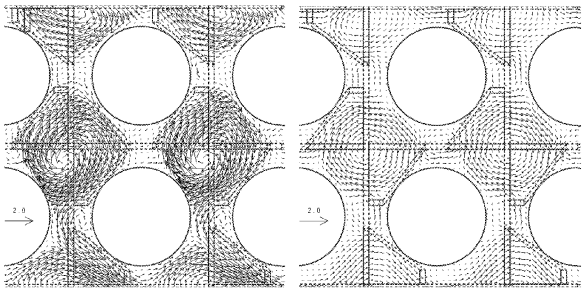

(a) (b)

Figure 7: Mean lateral flow pattern downstream of spacer grid at (a) $x = 8$ and (b) $x = 16$ (every 5th grid is shown). The reference arrow indicates $2u_\tau$.

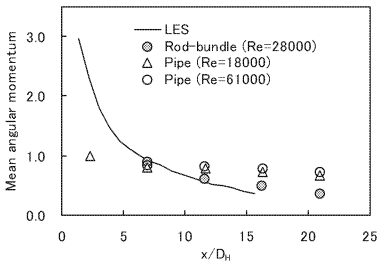

Figure 8: Axial variation of mean angular momentum: Ω. The angular momentum is normalized by the value at $x = 6.3D_H/P$. The result of LES ranges from the top of mixing-vane to the bottom of strap.

Table 1: Constants for Lamb-Oseen votex

x	Γ_0	$1/4\nu t$
7.9	1.4	20
9.4	1.2	18
15	0.8	14

DISCUSSION

Axial variations of mean azimuthal velocities and circulations are shown in Fig.9. The data at $x = 7.9$, 9.4 and 15 are selected to show typical parts of developed swirl. In this figure, the results of LES are compared with those of Lamb-Oseen vortex:

$$\overline{u_\theta} = \frac{\Gamma_0}{2\pi r}\left(1 - e^{-r^2/4\nu t}\right) \tag{10}$$

where Γ_0 is the circulation at the limit of radial infinity (Saffman, 1992). The values of Γ_0 and $1/4\nu t$ are adjusted for the curve to fit the result of LES. The adjusted values normalized by P and u_τ are shown in Table1. The decrease in Γ and $1/4\nu t$ in the downstream direction is caused by the turbulence stress. In addition, Lamb-Oseen vortex cannot reproduce the profiles in the outer region. This discrepancy is due to the difference in the boundary conditions; namely, no-slip for the rod wall and shear-free for the rod gap in our case.

In order to consider the effect of turbulence stress and boundary condition on Lamb-Oseen vortex, we formulate the circulation for viscous and turbulence stresses. Assuming that the mean velocities are symmetric on channel center and independent on axial direction, the momentum equation for the mean azimuthal velocity becomes:

$$\frac{\partial \overline{u_\theta}}{\partial t} = \nu\left(\frac{\partial^2 \overline{u_\theta}}{\partial r^2} + \frac{1}{r}\frac{\partial \overline{u_\theta}}{\partial r} - \frac{\overline{u_\theta}}{r^2}\right) - \frac{1}{r^2}\frac{\partial}{\partial r}\left(r^2\overline{u_r' u_\theta'}\right) \tag{11}$$

Assuming the steady state and multiplying by r^2 derives:

$$\frac{\nu}{2\pi}\frac{\partial \Gamma_r}{\partial r} = \frac{\partial}{\partial r}\left(r^2\nu\frac{\partial \overline{u_\theta}}{\partial r}\right) - \frac{\partial}{\partial r}\left(r^2\overline{u_r' u_\theta'}\right) \tag{12}$$

where $\Gamma_r = 2\pi r\overline{u_\theta}$. By this definition, the circulation of the swirl shown in Fig.9 is represented by a negative value of Γ_r. Equation (12) indicates that the diffusion of angular momentum balances with that of viscous and turbulence stress. To

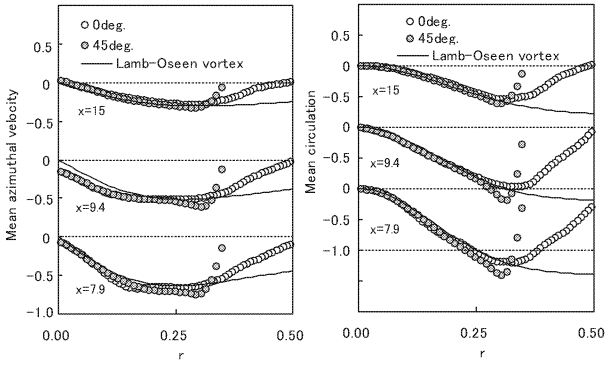

(a) (b)

Figure 9: Axial variations of mean (a) azimuthal velocities: $\overline{u_\theta}$ and (b) circulations: $\Gamma = \Gamma_0(1 - e^{-r^2/4\nu t})$.

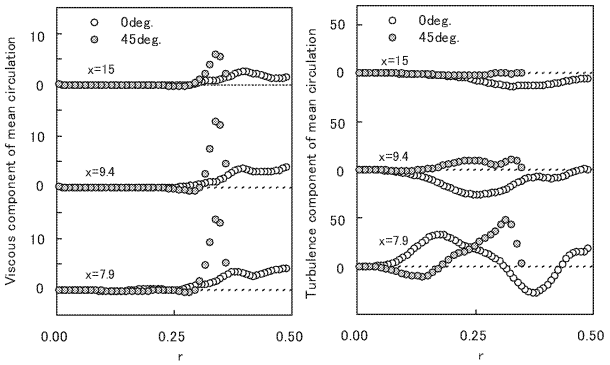

(a) (b)

Figure 10: Axial variations of the contribution of viscous and turbulence stresses to the circulation of swirl. (a) Viscous stress: $2\pi r^2 \partial\overline{u_\theta}/\partial r$, (b) turbulence stress: $2\pi r^2 \overline{u_r' u_\theta'}/\nu$.

clarify this effect on the circulation of Lamb-Oseen vortex, integrating Equation (12) and letting Γ_r, $\partial\overline{u_\theta}/\partial r$ and $\overline{u_r' u_\theta'} \to 0$ as $r \to 0$ based on the radial symmetry derive:

$$\Gamma_r = 2\pi r^2 \left(\frac{\partial \overline{u_\theta}}{\partial r} - \frac{1}{\nu} \overline{u_r' u_\theta'} \right) \tag{13}$$

This formulation is useful for the discussion about the effect of turbulence stress and boundary condition.

The contribution of each term in the right-hand side of Equation (13) is shown in Fig.10. The diffusion by viscous stress becomes evident near the rod wall for 45 degrees and in the rod gap for 0 degree. The contribution of turbulence stress for 0 degree is different from that for 45 degrees. For 45 degrees, the turbulence stress contributes negatively near the rod wall; this corresponds to the positive correlation of u_r' and u_θ': $u_r' > 0$ in the swirl produces $u_\theta' > 0$ decelerating the swirl; the angular momentum of the swirl is diffused at the rod wall vertical to the radial direction; this is the same for the swril in a pipe. For 0 degree, the contribution in $x = 7.9$ is different from that in $x = 9.4$ and 15. In the downstream ($x = 9.4$ and 15), the turbulence stress contributes positively near the rod gap; this corresponds to the negative correlation of u_r' and u_θ': $u_r' > 0$ in the swirl produces $u_\theta' < 0$ promoting the swirl; the radial component of the angular momentum is transferred azimuthally at the curved rod wall not vertical to the radial direction. In the upstream ($x = 7.9$), the turbulence stress contributes negatively in the core region; this positive correlation of u_r' and u_θ' is a result of the balance of angular momentum distributed between the swirl in the core region and the vortex in the rod gap (see Fig.7(a)). We think this is the main reason for the swirl in rod-bundle decays faster than that in a pipe.

CONCLUSION

We carried out an LES of swirled turbulent flow in rod-bundle. In order to treat complicated geometry, we used an improved immersed boundary method and a new one-equation dynamic SGS model. The complex geometry effect on the velocity field was accurately simulated by means of the immersed boundary method with the higher-order forcing and consistent correction. The new one-equation dynamic SGS model was useful for this complex geometry because the dynamic procedure requires neither the near-wall correction for SGS viscosity nor the average of dynamic parameter.

The computational results reasonably reproduced previous data obtained by experiments and computations. The results were able to represent the effect of flow geometry: the flow around mixing-vanes causes the swirl and the large-scale fluctuation enhancing heat transfer; turbulence stress promotes the decay of the swirl more strongly than in a pipe; but it produces a vortex in rod gap enhancing enthalpy mixing between channels. Our formulation for the viscous and turbulence stresses was useful for the developed swirl and will be for the swirl indicating significant decay near the mixing-vanes. These results suggested that LES technique become a useful tool for designing the spacer grid by predicting the effect of flow control.

REFERENCES

Ikeno,T., Kajishima,T., 2003a, "Large eddy simulation of fully developed sub-channel turbulence", *Proceedings of international topical meeting on Nuclear Reactor Thermal Hydraulics*, Seoul, A00601, [CD-ROM].

Ikeno, T., Kajishima, T., 2003b, "Higher-order immersed boundary method for LES with complicated boundaries", *Transactions of JSME*, B, Vol.69, No.686, pp.2177-2183, [in Japanese].

Ikeno,T., Kajishima,T., 2004, "Difference formula of Poisson equation consistent with an immersed boundary method", *Transactions of JSME*, B, Vol.70, No.697, pp.2239-2245, [in Japanese].

In,W.K., Oh,D.S., Chun,T.H. 2003, "Simulation of turbulent flow in rod bundles using eddy viscosity models and the Reynolds stress model", *Proceedings of international topical meeting on Nuclear Reactor Thermal Hydraulics*, Seoul, 48, E00213, [CD-ROM].

Kajishima,T., 1994, "Conservation properties of finite difference method for convection", *Transactions of JSME*, B, Vol.60, No.574, pp.2058-2063, [in Japanese].

Kajishima,T., and Nomachi,T., 2003, "Applying dynamic procedure for the energy production in one-equation subgrid scale model of LES", *Proceedings of 3rd International Symposium on Turbulence and Shear Flow Phenomena*, Sendai, pp.651-656

Kreith,F., Sonju,O.K., 1965, "The decay of a turbulent swirl in a pipe", J.Fluid Mech., Vol.22, pp.257-271.

McClusky,H.L., Holloway,M.V., Beasley,D.E, 2002, "Developement of swirling flow in a rod bundle subchannel", *ASME Journal of Fluids Engineering*, Vol.124, pp.747-755.

Mohd-Yusof,J, 1997, "Combined immersed boundary / B-spline methods for simulations of flows in complex geometries", *CTR annual research briefs*, NASA Ames / Stanford Univ., pp.317-327.

Perot,J.B., 1993, "An analysis of the fractional step method", *J.Comput.Phys.*, Vol.108, pp.51-58

Rehme, K., 1992, "The structure of turbulence in rod bundles and the implications on natural mixing between the subchannels", *Int. J. Heat Mass Transfer*, Vol.35, pp.567-581

Saffman,P.G, 1992, *Vortex Dynamics*, Cambridge University Press, United Kingdom.

Yang,S.Y., Chung,M.K., 1996, "Spacer grid effects on turbulent flow in rod bundles", *J.Korean Nuclear Society*, Vol.28, No.1, pp.56-71